Title
Simulation of electrospray emission processes for low to moderate conductivity liquids

Journal
Physics of Fluids, 34(11)

ISSN
1070-6631

Authors
Huh, Henry
Wirz, Richard E

Publication Date
2022-11-01

DOI
10.1063/5.0120737

Physics of Fluids

Simulation of electrospray emission processes for low to moderate conductivity liquids

Cite as: Phys. Fluids **34**, 112017 (2022); https://doi.org/10.1063/5.0120737
Submitted: 14 August 2022 • Accepted: 05 October 2022 • Accepted Manuscript Online: 06 October 2022 • Published Online: 15 November 2022

Henry Huh and Richard E. Wirz

Physics of Fluids ARTICLE scitation.org/journal/phf

Simulation of electrospray emission processes for low to moderate conductivity liquids

Cite as: Phys. Fluids **34**, 112017 (2022); doi: 10.1063/5.0120737
Submitted: 14 August 2022 · Accepted: 5 October 2022 ·
Published Online: 15 November 2022

Henry Huh[a] and Richard E. Wirz[b]

AFFILIATIONS

Department of Mechanical and Aerospace Engineering, University of California Los Angeles, Los Angeles, California 90095, USA

[a]Electronic mail: HenryHuh89@ucla.edu
[b]Author to whom correspondence should be addressed: wirz@ucla.edu

ABSTRACT

The leaky-dielectric model is incorporated in the Finite Volume Method (FVM) code, OpenFOAM, to investigate the electrospray emission behavior of low to moderate conductivity liquids. This work extends FVM modeling to moderate conductivities by employing a new interface interpolation scheme that is devised in the volume of fluid method to ensure charge conservation for accurate reproduction of charge accumulation and resulting meniscus shape in the cone-to-jet region and jet breakup. The model results agree well with experiments and scaling laws for droplet diameter and total current for low and moderate conductivity fluids, i.e., heptane and tributyl phosphate, respectively. The droplet diameter is shown to increase as the dimensionless flow rate increases or the electric Reynolds number decreases. The results are also consistent with a parametric investigation of the meniscus shape and the maximum charge density for key operating conditions (flow rate and extraction potential) and liquid properties (conductivity, surface tension, viscosity, and relative permittivity). These results show that the new interface interpolation scheme provides accurate results for a wide range of conductivities, fluid properties, and operating conditions. The results also provide valuable physical insight for varying liquid conductivity in the electrospray emission process. In particular, low dimensionless flow rate or high electric Reynolds number leads to the emergence of convex-outward menisci associated with a high charge density in the cone-to-jet region, resulting in high jetting velocity and high specific charge droplets.

I. INTRODUCTION

Electrosprays are attractive for many applications, such as mass spectrometry, MEMS fabrication, nano-fiber deposition, and electric propulsion (EP). In the last few decades, considerable study has been undertaken to understand the underlying physics of electrohydrodynamics (EHD) in an electrospray. A potential difference of hundreds to several thousand volts is typically applied between an emitter and an extraction electrode, producing a cone-shaped meniscus that can lead to a liquid jet, droplets, and ions in the operation of an electrospray.

A conical meniscus is developed by surface tension and electrostatic forces balanced on the interface in the cone-jet mode. Zeleny first observed different modes of electrosprays including the steady cone-jet mode, which has been of significant interest for stable emission of droplets.[1] Cloupeau and Prunet-Foch examined various cone-jet structures and operating modes experimentally in a range of operating conditions and physical properties of low to moderate conductivity liquids[2] (2×10^{-8} to 1×10^{-4} S m^{-1}). Taylor applied electrostatic analysis for perfectly conductive liquid up to the location where a jet begins to develop from the cone;[3] the half cone-angle at the apex was shown to be 49.3°. The Ohmic, leaky-dielectric model of Melcher and Taylor supplements Taylor's analysis by introducing tangential electrostatic force due to free charge accumulation at the liquid interface, unlike in perfect conductors and dielectrics involving perpendicular electrical stress.[4] Pantano *et al.* solved the zeroth-order electrostatic equations from the theory of Taylor to observe the effect of charge accumulation on the cone-jet formation.[3,5] They acquired the meniscus shape with a conical tip for the first time assuming the vertex angle as 49.3°. The charge accumulation at the tip of the meniscus allows high enough electrostatic force dominating over the surface tension force in the cone-to-jet region. Furthermore, a concave-outward meniscus transitions to a convex meniscus with the decreasing Taylor's number, $\frac{\varepsilon_0 \phi_0^2}{2\gamma D_e}$, where ε_0, ϕ_0, γ, and D_e are the vacuum permittivity, potential relative to the ground electrode, surface tension coefficient, and outer diameter of the electrode, respectively.[5]

Important scaling relationships have been developed to correlate the output parameters of interest under different assumptions.[6–8] Although they provide valuable physical insight, the scaling laws

cannot describe the emission mechanics during evolution of a cone-jet and subsequent droplet breakup. Several numerical models have been developed to describe the process of cone-jet formation and electrospray emission. The boundary element/integral method (BEM) is computationally cost-efficient and allows accurate analysis under the given constraints.[5,9,10] Higuera investigated the surface charge density with varying flow rates and permittivities with the far-field boundary condition obtained from electrostatic solution[3] in the restricted cone-to-jet region.[9] Herrada and Montanero applied Newton–Raphson method to solve the nonlinear discrete equations and observed nonlinear dynamics of a liquid bridge at the minimum volume stability limit.[11] Ponce-Torres *et al.* applied the boundary fitted method to calculate the base flow and the corresponding eigenmodes to determine the linear global modes of the system.[12] Gamero-Castaño and Magnani went further to obtain solution in an extended cone-to-jet region,[10] concluding the surface position of tributyl phosphate (TBP) largely invariant to physical properties and flow rates for dielectric constants of 8.91 and 64.9. The current boundary element/fitted methods cannot make prediction of emitted droplets or internal flow in bulk liquid, which are important observable parameters in electric propulsion.

The finite volume method (FVM) allows robust handling of nonlinear conservation equations as a more flexible approach than the BEM. The FVM can reproduce not only the cone-jet structure but also downstream breakup and emitted droplets in an electrospray.[13,14] Several EHD models have been developed on the basis of the FVM. López-Herrera *et al.* and Herrada *et al.* used the volume-of-fluid method to track interfaces in a multiphase problem by an open source tool, Gerris.[15–17] Roghair *et al.* developed an EHD OpenFOAM solver based on the work of López-Herrera *et al.*, which was extended by Dastourani *et al.* to simulate electrosprays of low conductivity ($\sim 1 \times 10^{-8}$ to $\sim 1 \times 10^{-6}$ S m^{-1}) liquid.[13–15] Complex emitter geometry, such as a porous emitter, is effectively modeled by the CVFEM (control volume finite element method) for high conductivity liquid where self-heating can be significant.[18–20] More recently, Guan *et al.* applied OpenFOAM for modeling pulsating electrospray emission with no droplet breakup in a steady cone-jet mode at low electric Bond numbers.

The objective of this study is to develop a high-fidelity EHD model that can provide detailed emission mechanism for electrospray devices in a wide range of operating conditions and fluid properties. A new interface interpolation scheme is developed and shown to effectively suppress charge lass and simulate jet breakup, thus extending the modeling capabilities up to moderate conductivity ($\sim 10^{-4}$ S m^{-1}) liquids while still providing accurate results for lower conductivity ($\sim 10^{-7}$ S m^{-1}). We will validate the suggested models against experimental observations and scaling relationships. In particular, we run the model across the operating conditions and the fluid properties critical in defining the steady cone-jet mode. We show how the charge distribution varies along the interface and how the meniscus shape is determined by the competing electrostatic and surface tension forces on the interface. The governing equations are discussed in Sec. II and numerical methods in Sec. III. The modeling results for the low conductivity liquid are presented in Sec. IV A and those for the moderate conductivity liquid in Sec. IV B. The concluding remarks are provided in Sec. V.

II. MODEL FORMULATION

A. Fluid flow

Electrohydrodynamic fluid flow is governed by the incompressible continuity and momentum equations given as

$$\nabla \cdot \boldsymbol{u} = 0, \tag{1}$$

$$\rho\left[\frac{\partial \boldsymbol{u}}{\partial t} + \boldsymbol{u} \cdot \nabla \boldsymbol{u}\right] = -\nabla \boldsymbol{P} + \mu \nabla^2 \boldsymbol{u} + \rho \boldsymbol{g} + \boldsymbol{F}_E + \boldsymbol{F}_{ST}, \tag{2}$$

where $\boldsymbol{u}$, t, ρ, $\boldsymbol{P}$, and μ represent velocity, time, density, pressure, and dynamic viscosity, respectively. Note that the electrostatic force, $\boldsymbol{F}_E$, and the surface tension force, $\boldsymbol{F}_{ST}$, are added to the momentum equation.[15] Here, $\boldsymbol{F}_{ST}$ is given as

$$\boldsymbol{F}_{ST} = \gamma \kappa \nabla \alpha = \gamma(-\nabla \cdot \hat{\boldsymbol{n}}) \nabla \alpha, \tag{3}$$

$$\hat{\boldsymbol{n}} = \frac{\nabla \alpha}{|\nabla \alpha| + \delta'}, \tag{4}$$

where the surface tension term is reformulated according to the continuum surface force (CSF) model by Brackbill *et al.*[21] γ is the surface tension coefficient, κ is the interface curvature, and $\hat{n}$ is the unit normal vector. δ' is a small number relative to $|\nabla \alpha|$ to ensure a non-zero denominator in Eq. (4).

The volume of fluid (VOF) method captures the interface between liquid and vacuum by using a Heaviside function of the liquid volume fraction,[22] α_{liq}. Each computational cell is represented as $\alpha_{liq} = 0$ within gas or vacuum, $\alpha_{liq} = 1$ within liquid, and $0 < \alpha_{liq} < 1$ at the interface. The liquid volume fraction is calculated by solving the transport equation given as

$$\frac{\partial \alpha_{liq}}{\partial t} + \nabla \cdot (\boldsymbol{u} \alpha_{liq}) + \nabla \cdot (\alpha_{liq}(1 - _{liq}) \boldsymbol{u}_{\boldsymbol{r}}) = 0, \tag{5}$$

$$\boldsymbol{u}_{\boldsymbol{r}} = C_{alpha} \left| \frac{\phi_a}{|S_a|} \right| \hat{\boldsymbol{n}}, \tag{6}$$

where $\boldsymbol{u}_{\boldsymbol{r}}$ is an artificial compression term for sharpness of the interface.[23] ϕ_a, S_a, and C_{alpha} are velocity flux, face surface area, and an adjustable compression factor. C_{alpha} is set to unity here, whereas it is between 0 and 4 in most practical cases. Large C_{alpha} allows a sharp interface but increases the magnitude of possible spurious current.[24,25] In the conventional VOF method, a cell-averaged property, ψ, such as density, viscosity, electrical conductivity, or permittivity is calculated as

$$\psi = \psi_1 \alpha_{liq} + \psi_2 (1 - \alpha_{liq}) \quad \text{for} \quad \psi \in [\rho, \nu, \sigma, \varepsilon], \tag{7}$$

where ψ_1 and ψ_2 are the properties of liquid and vacuum, respectively. The interface is reconstructed according to the liquid volume fraction, α_{liq}, and solution of the transport equations for all relevant cell-averaged properties.

B. Electrostatics

The volumetric electrostatic force, $\boldsymbol{F}_E$, is described by the Maxwell's equations which are reduced to the electrostatic equation with negligible magnetic effect in Eq. (8). The Gauss's law is given in Eq. (9) as

$$\nabla \times \boldsymbol{E} = 0, \tag{8}$$

$$\nabla \cdot (\varepsilon \boldsymbol{E}) = \rho_e, \tag{9}$$

where $\boldsymbol{E}$ is the electric field vector, ε is the electrical permittivity, and ρ_e is the volumetric charge density. The charge conservation equation,

$$\frac{\partial \rho_e}{\partial t} + \nabla \cdot \boldsymbol{J} = 0, \tag{10}$$

is converted to Eq. (11) by substituting the current density, $\boldsymbol{J}$, as the sum of Ohmic conduction and charge convection as $\boldsymbol{J} = \sigma \boldsymbol{E} + \rho_e \boldsymbol{u}$,

$$\frac{\partial \rho_e}{\partial t} + \nabla \cdot (\rho_e \boldsymbol{u}) = -\nabla \cdot (\sigma \boldsymbol{E}). \tag{11}$$

The electrostatic force is given as the sum of Coulombic and polarization forces as

$$\boldsymbol{F}_E = \rho_e \boldsymbol{E} - \frac{1}{2}\boldsymbol{E}^2 \nabla \varepsilon, \tag{12}$$

which acts on the electric charge accumulated on the surface of an electrospray. Important dimensionless parameters are defined as follows: the dimensionless flow rate, δ, in Eq. (13), the electric Reynolds number, Re_E, in Eq. (14), and the electric Bond number, B_E, in Eq. (15), where Q is the flow rate, ε_0 is the vacuum permittivity, V_0 is the emitter voltage, and R_0 is the outer radius of the emitter,

$$\delta = \frac{\rho \sigma Q}{\gamma \varepsilon_0}, \tag{13}$$

$$Re_E = \left(\frac{\rho \varepsilon_0 \gamma^2}{\mu^3 \sigma}\right)^{\frac{1}{3}}, \tag{14}$$

$$B_E = \frac{\varepsilon_0 V_0^2}{R_0 \gamma}. \tag{15}$$

III. NUMERICAL METHODS

The open source code, OpenFOAM, is based on the FVM to obtain linearized relationships among neighboring cell-averaged variables of the governing equations.[26] The second-order-accurate linear upwind scheme is employed to suppress false diffusion due to the discretized convection term.[27,28] As the velocity boundary conditions, a fixed uniform value is applied at the inlet, the zero-gradient condition at the outlet and the wall, the symmetry condition on the axis, and the cyclic boundary condition at the front and the back of the wedge-shaped three-dimensional domain. Similarly, as the pressure boundary condition, the zero-gradient is applied at the inlet and zero total pressure at the outlet and on the wall to maintain vacuum in the domain. The electrospray emission behaviors have been reported to be in the steady cone-jet mode for heptane and tributyl phosphate in this study.[29,30] Measurements have shown the flow to be axisymmetric below the threshold when the jet begins whipping at high electric Reynolds number or low non-dimensional flow rates.[12,31] We limit the scope of our study to the steady cone-jet mode at moderate electric Reynolds number where axisymmetric modes are dominant. Sensitivity study is performed to determine the total number of mesh cells, N_c, large enough to show no further dependence of the computed results on the grid size. N_c is set equal to 138 800 for the low conductivity case and 98 990 for the moderate conductivity case, where the droplet diameter converges to 15.6 μm for heptane and 6 μm for TBP in Fig. 2(a). The average computational time step for each iteration is about 2.3×10^{-8} s, and 5.7×10^{-9} s for heptane and TBP. The final residuals of U_x, U_y, and U_z are 9.6×10^{-11}, 9.0×10^{-11}, and 9.8×10^{-11} m s^{-1}, respectively, and the residual for pressure is 1.5×10^{-6} kg/m s^2. We applied adaptive time stepping based on the maximum allowed Courant number, which was 0.5 for both heptane and tributyl phosphate per the CFL (Courant-Friedrichs-Lewy) condition.

The VOF method is employed to reconstruct the interface to capture the interfacial forces on the jet and the cone meniscus.[32,33] Preliminary results showed importance of avoiding false leakage of mass and charge through appropriate treatment of the cell-averaged quantities at the liquid–vacuum interface. Tomar *et al.*; López-Herrera *et al.* used the weighted arithmetic mean (WAM) for two-phase σ and ε based on their linear weighted averages in terms of the liquid volume fraction.[15,34] In our simulation, the WAM led to significant numerical diffusion with no droplet breakup occurring for moderate to high conductivity liquids. López-Herrera *et al.* investigated the interpolation schemes, weighted arithmetic mean (WAM), and weighted harmonic mean (WHM), concluding that the WHM does not provide any better accuracy for moderately conductive dielectric-conducting liquid.[15] The WHM essentially assigns zero conductivity to all cells involving liquid–vacuum interface to result in code failure due to the abrupt change in the physical properties between neighboring cells. In this study, we devised a new interpolation scheme in Eqs. (16) and (17) to determine the cell-averaged conductivity and permittivity in every two-phase cell involving the interface. Note that Eqs. (16) and (17) reduce to the WAM for $f = 1$ and to the WHM for $f = -1$,

$$\sigma_{cell} = (\alpha_{liq}\sigma_{liq}^{1/f} + (1 - \alpha_{liq})\sigma_{vac}^{1/f})^f, \tag{16}$$

$$\varepsilon_{cell} = (\alpha_{liq}\varepsilon_{liq}^{1/f} + (1 - \alpha_{liq})\varepsilon_{vac}^{1/f})^f, \tag{17}$$

where σ_{cell} and ε_{cell} are the cell averaged quantities, while the subscripts, liq and vac, represent liquid and vacuum, respectively. Here, σ_{vac} is equal to zero and ε_{vac} is equal to the vacuum permittivity, ε_0. The liquid volume fraction and the corresponding charge density are shown for $f = 1$(WAM) and $f = 20$ in Fig. 1. Linear interpolation for the WAM results in smoothly varying σ and ε with significant false diffusion and leakage through the interface. Note the erroneous results by the WAM showing excessive droplet sizes and failure in charge conservation for heptane in Fig. 1. Note that the charge is well conserved to result in converged droplet diameters showing no further dependence on f for $f > 20$ in Fig. 2(b). It was a compromise between smooth resolution without code failure and a sharp interface with suppressed numerical diffusion. A larger f better reproduces sharp variation of σ and ε with less false diffusion, leading to a finer jet and smaller droplets. The maximum charge density is $\rho_{E,\max} = 430\,\mathrm{C/m^3}$ for $f = 20$ and $\rho_{E,\max} = 60\,\mathrm{C/m^3}$ for $f = 1$ in Fig. 1. Obviously finer grids will be required for better resolution accuracy and numerical stability for electrosprays of high conductivity liquids.

IV. RESULTS AND DISCUSSION

The computational domain covers the region from emitter to extractor both in Tang and Gomez (Sec. IV A) and Gamero-Castaño and Hruby (Sec. IV B).[29,30] Simulation is based on the published experimental setups with the given physical properties and operating conditions including flow rate and voltage. Photographs in Fig. 3 show the experimentally observed cone-jet formation and emitted droplets for heptane of low conductivity. Relevant physical properties are listed for heptane and TBP in Table I.

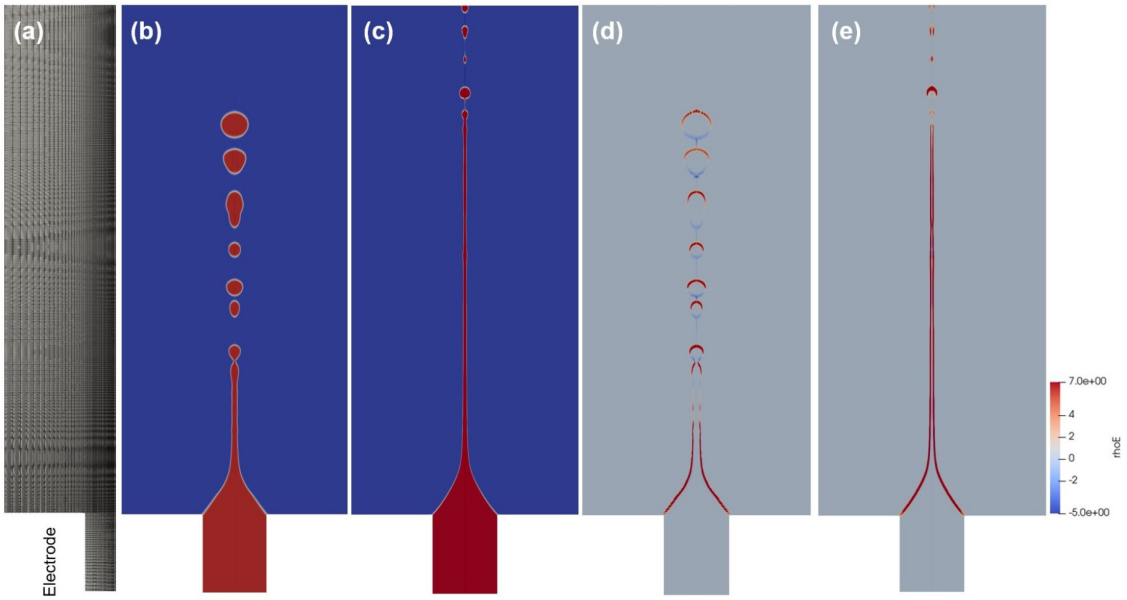

FIG. 1. Comparison of the WAM and the new interpolation scheme for heptane: (a) computational domain, (b) liquid volume fraction for $f = 1$ (WAM), (c) liquid volume fraction of $f = 20$, (d) charge density for $f = 1$, and (e) charge density for $f = 20$.

The total current, I, in an electrospray includes the two contributions by charge conduction and convection to be given as

$$I_{total} = \int_S (\sigma \boldsymbol{E} + \rho_e \boldsymbol{u})\, d\boldsymbol{S}, \tag{18}$$

where $\boldsymbol{S}$ is the cross-sectional surface of the cone-jet. We define the cone-to-jet length, L_{cj}, as the region where the convective current changes from 5% to 95% of its final value. It corresponds to the transition region in Gamero-Castaño and Magnani and the charge relaxation region in De La Mora and Loscertales.[8,10] The charge relaxation time is defined as $\tau_e = \frac{\varepsilon}{\sigma}$.

A. Low conductivity liquid

Figure 3 shows experimental observations of cone-jet formation and droplet breakup of heptane.[29] Figures 4(a) and 4(b) show the computational domain and grid for the experimental setup in Tang and Gomez.[29] The nozzle and outer diameters are 120 and 450 μm, the orifice diameter is 12 mm, and the distance between emitter and extractor is 29.8 mm. Figures 4(c) and 4(d) show the computed distributions of liquid volume fraction and contour and magnitude of the electric field on a 2D plane through the axis. Note the concave-outward meniscus in the qualitative agreement with the experimental observations in Figs. 3(a) and 3(b). Note the maximum electric field at the cone-to-jet region well below the minimum threshold for ion emission[35] ($\sim 1 \times 10^9$ V m^{-1}). Scaling relationships by Gañán Calvo are given for the dimensionless droplet diameter and the total current,[6] respectively, in Eqs. (19) and (20). Another scaling relationship by De La Mora and Loscertales is given for the dimensionless droplet diameter[8] in Eq. (21). ε_r is the relative permittivity. These scaling relationships apply only to the steady cone-jet mode

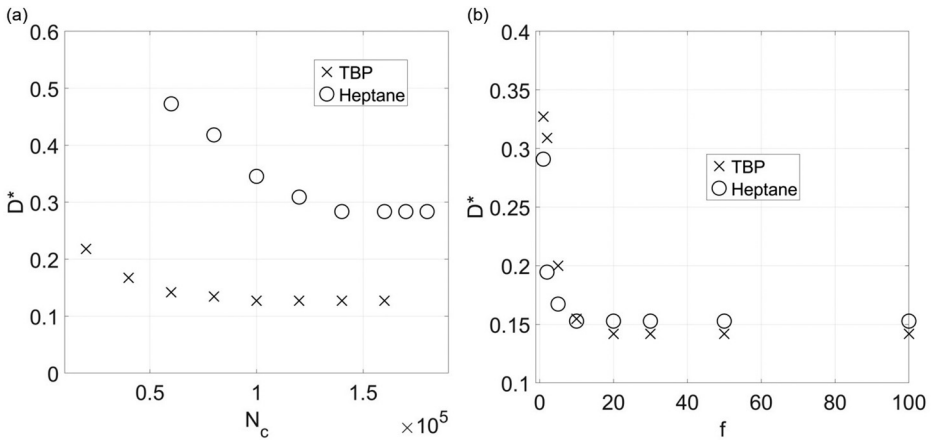

FIG. 2. Sensitivity analysis for the dimensionless droplet diameter, D^*, with respect to (a) the number of cells, N_c, and (b) the parameter f.

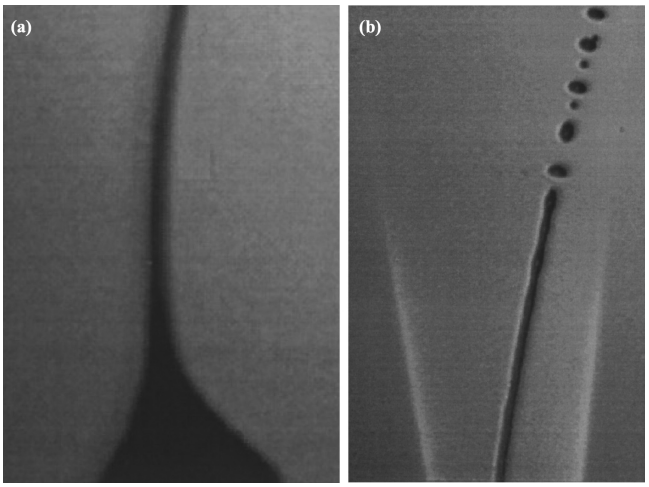

FIG. 3. Photographs of (a) cone-jet formation and (b) emitted droplets for heptane of low conductivity[29] ($\sigma = 6.26 \times 10^{-7}$ S m^{-1}). Reproduced with permission from Tang and Gomez, J. Colloid Interface Sci. **184**, 500–511 (1996). Copyright 1996 Elsevier.

$$D = \left(\frac{\rho\varepsilon_0 Q^3}{\sigma\gamma}\right)^{\frac{1}{6}}, \tag{19}$$

$$I = (\gamma\sigma Q)^{\frac{1}{2}}, \tag{20}$$

and

$$D = \left(\frac{\varepsilon_r\varepsilon_0 Q}{\sigma}\right)^{\frac{1}{3}}. \tag{21}$$

D^* in Figs. 5 and 8 is the mean droplet diameter normalized by the inner diameter of the emitter. In Fig. 5(a), $1/Re_E$ ranges from 0.03 to 0.068 for the dimensionless flow rate varying between $\delta = 2.4$ and $\delta = 9.7$. In Fig. 5(b), the electric Bond number is varied from 71 to 198 for the dimensionless flow rates of 13.9, 46.4, and 69.6 for $\gamma = 0.0186$ N m^{-1} according to Tang and Gomez. The reasonable agreement is shown with proper trends of variation of D^* for model predictions, scaling laws, and experimental observations in Fig. 5. The mean droplet diameter is compared with the universal scaling law in the steady cone-jet mode in Eq. (19) and the experimental results in Tang and Gomez. The droplet size was reported to decrease with decreasing Re_E, decreasing flow rate, and increasing B_E as previously discussed in the literature.[6–8,14,29,30] In Fig. 5(b), although Eqs. (19) and (21) are given as functions of the flow rate and physical properties only, the measured and computed droplet diameters show strong dependence on the emitter voltage with the increasing flow rate. The computed modeling results show the droplet diameter reduced by about 30% with the increase in the B_E from 71 to 127 at the lowest flow rate, $\delta = 13.9$, in Fig. 5(b).

TABLE I. Liquid properties of heptane and tributyl phosphate (TBP).[29,30]

Liquid	ρ(kg/m^3)	σ(S/m)	γ(N/m)	ε(F/m)	μ(m^2/s)
Heptane	684	6.26×10^{-7}	0.0186	1.91	4.28×10^{-4}
TBP	976	2.3×10^{-4}	0.028	8.91	3.59×10^{-3}

Figure 6 shows distributions of the cone radius, R, and the charge density, ρ_E^*, along the meniscus for varying operating conditions and liquid properties about the reference condition, $Q = 0.5$ mm^3/s, $V = 4$ kV. ρ_E^* is the volumetric charge density nondimensionalized by $\frac{(\gamma\sigma Q)^{\frac{1}{2}}}{\pi d_1^2 v_s}$, where $v_s = \frac{Q}{\pi d^2}$ is the scaling parameter for jet velocity.[7] In Fig. 6(a), the flow rate decreasing from $Q = 2.5$ mm^3/s to $Q = 0.5$ mm^3/s results in a steeper meniscus induced by increasing tangential electric field and increasing charge density according to the Gauss's law in Eq. (9). Note the electric field magnitude increasing exponentially as the flow rate decreases, as given in Gamero-Castaño.[35] A high charge density leads to a high F_E in Eq. (12) resulting in a fine jet and small droplets with a short L_{cj}. Likewise, the increase in γ from 0.01 to 0.05 N m^{-1} results in transition from a concave to a flattened meniscus. Note the largest ρ_E^* and the shortest L_{cj} at the largest γ of 0.05 N m^{-1} in Fig. 6(b). In Fig. 6(c), the tangential force increases with the increasing voltage up to 4.0 kV to result in a steeper meniscus leading to a finer jet and smaller droplet diameters. Note the menisci largely invariant with respect to the kinematic viscosity, ν, varying in the range between 6.3×10^{-7} and 5.0×10^{-5} m^2/s in Fig. 6(d). ρ_E^* also remains approximately the same, varying about 3% within the tested range of the kinematic viscosity. Note the largest viscosity, $\nu = 5.0 \times 10^{-5}$ m^2/s, resulting in a jet elongated up to the location, $z = 2\,\mu$m. The relative permittivity, ε_r, in Fig. 6(e) shows a different trend from those for varying δ, γ, V, and ν in Figs. 6(a)–6(d). High permittivity leads to a steep meniscus induced by the high polarization force, $-\frac{1}{2}\boldsymbol{E}^2\nabla\varepsilon$, increasing with ε_r, which is dominated by the effect of the low electrostatic force due to ρ_E^* lower by 64% for $\varepsilon_r = 50$ than that for $\varepsilon_r = 10$ in Fig. 6(e). It is due to a large charge relaxation time leading to decelerated charge transport and low ρ_E^* for the high permittivity case.

B. Moderate conductivity liquid

Figure 7 shows the setup and computed results for liquid volume fraction and electric field for TBP of moderate conductivity in Gamero-Castaño and Hruby.[30] It involves the nozzle inner and outer diameters of 110 and 230 μm, the diameter of the extractor orifice of 0.8 mm, and the distance between emitter and extractor equal to 2.5 mm. Note the maximum electric field of about 9.1×10^7 V m^{-1} at the cone-to-jet region, which is well below the minimum electric field of $\sim 10^9$ V m^{-1} required for ion emission.[35]

Figure 7 shows the meniscus shape and the magnitude of the electric field in the steady cone-jet mode. Note the smaller jet diameter and smaller droplets together with smaller cone-to-jet length due to higher charge density and stronger electric field than those for heptane in Fig. 4.

Figure 8 shows reasonable qualitative agreement of droplet diameters and total currents by experiment, modeling, and scaling laws in Eqs. (19)–(21). Deviation of the droplet diameters by modeling may indicate numerical uncertainty or underpredicted electrostatic force due to ignored viscous self-heating and temperature-dependent conductivity at a relatively low Reynolds number.[36,37] In experiment, droplets could fragment or undergo downstream influences such that droplets reaching the detector may not be those emitted off the jet.[38,39] Note in Fig. 8(b), the total current by modeling lying between those by

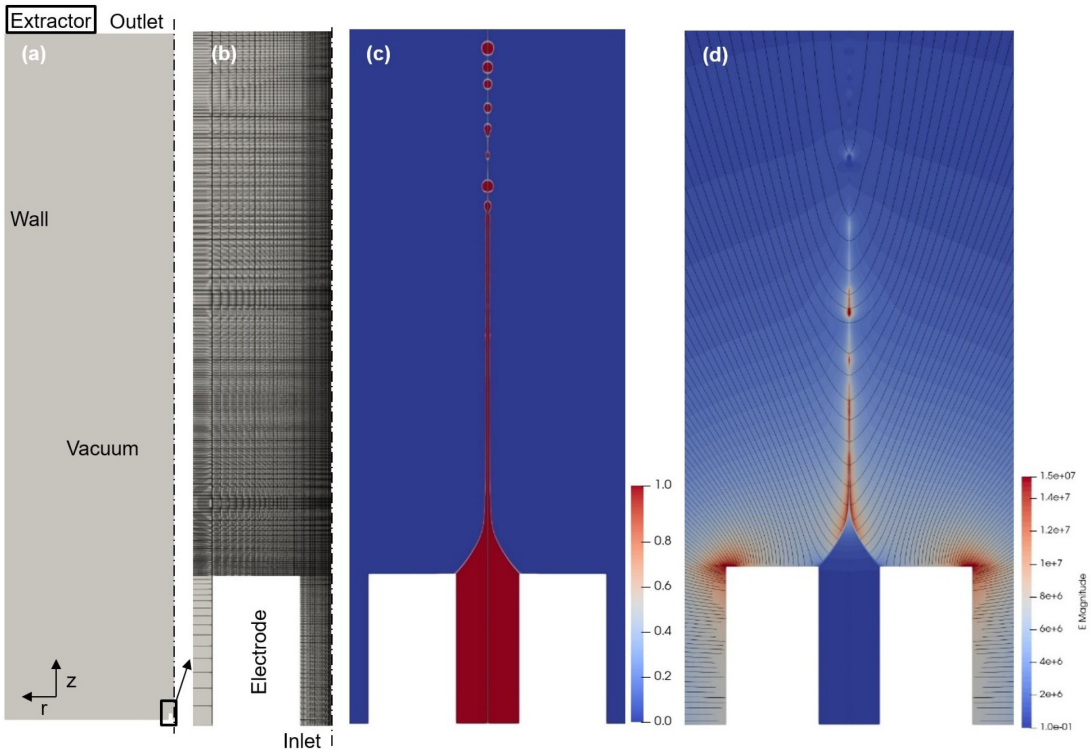

FIG. 4. Computation for heptane of low conductivity in steady cone-jet operation: (a) axisymmetric domain with 138 800 cells, (b) magnified emission region, (c) liquid volume fraction, and (d) magnitude and contour of the electric field.

the experiment[30] and scaling law proportional to a half-power of the flow rate in Eq. (20).

Figure 9 shows the cone radius and the charge density along the meniscus for varying δ, γ, and ε_r about the reference condition, $Q = 0.04\,\mathrm{mm^3/s}$ and $V = 1.7\,\mathrm{kV}$. Note a lower δ resulting in higher charge density so that the lowest $Q = 0.04\,\mathrm{mm^3/s}$ presents the highest ρ_E^* and the shortest L_{cj} in Fig. 9(a). At a lower flow rate, the jet may develop into the unstable whipping mode due to excessive electrostatic force as experimentally observed in Uchizono *et al.*[31] Similarly, γ increasing from 0.01 to $0.04\,\mathrm{N\,m^{-1}}$ results in increasing charge density with transition of the meniscus from concave to convex toward vacuum.

A scaling equation for the surface charge density, q_s, was derived from a quasi-one-dimensional analytical model as[40]

$$q_s = \varepsilon_0 E_0 = 0.62\left(\varepsilon_0 \gamma^2 \rho \sigma^2\right)^{\frac{1}{6}}, \tag{22}$$

which supports ρ_E^* increasing with increasing γ in Fig. 9(b). The change in ρ_E^* is associated with transition of the meniscus from convex $(\frac{\partial^2 R}{\partial Z^2} < 0)$ to concave-outward $(\frac{\partial^2 R}{\partial Z^2} > 0)$. Note the maximum ρ_E^* for $Q = 0.04\,\mathrm{mm^3/s}$ or $\rho_E^* = 2.5$ for $\gamma = 0.04\,\mathrm{N\,m^{-1}}$ nearly doubled as compared with the maximum ρ_E^* without such transition of the meniscus for higher δ's or lower γ's. Rapid increase in ρ_E^* with a short L_{cj} beyond the inflection point suggests that charge accumulation takes

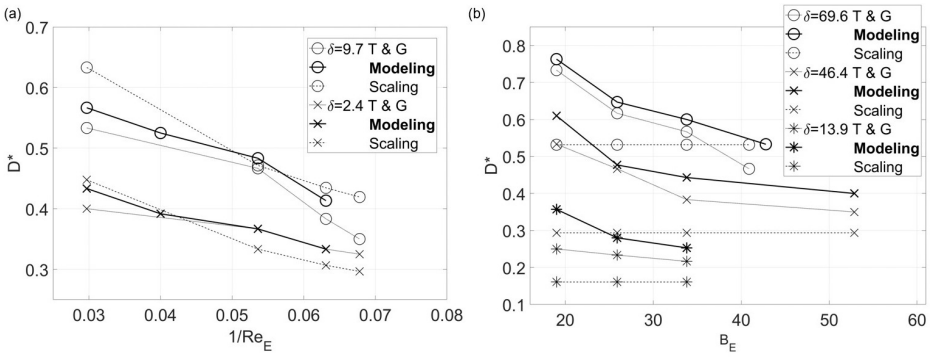

FIG. 5. Comparison of the dimensionless droplet diameters, D^*, by the experiment[29] (T & G), modeling and scaling[6] for heptane at different δ's with respect to (a) $1/Re_E$ and (b) B_E.

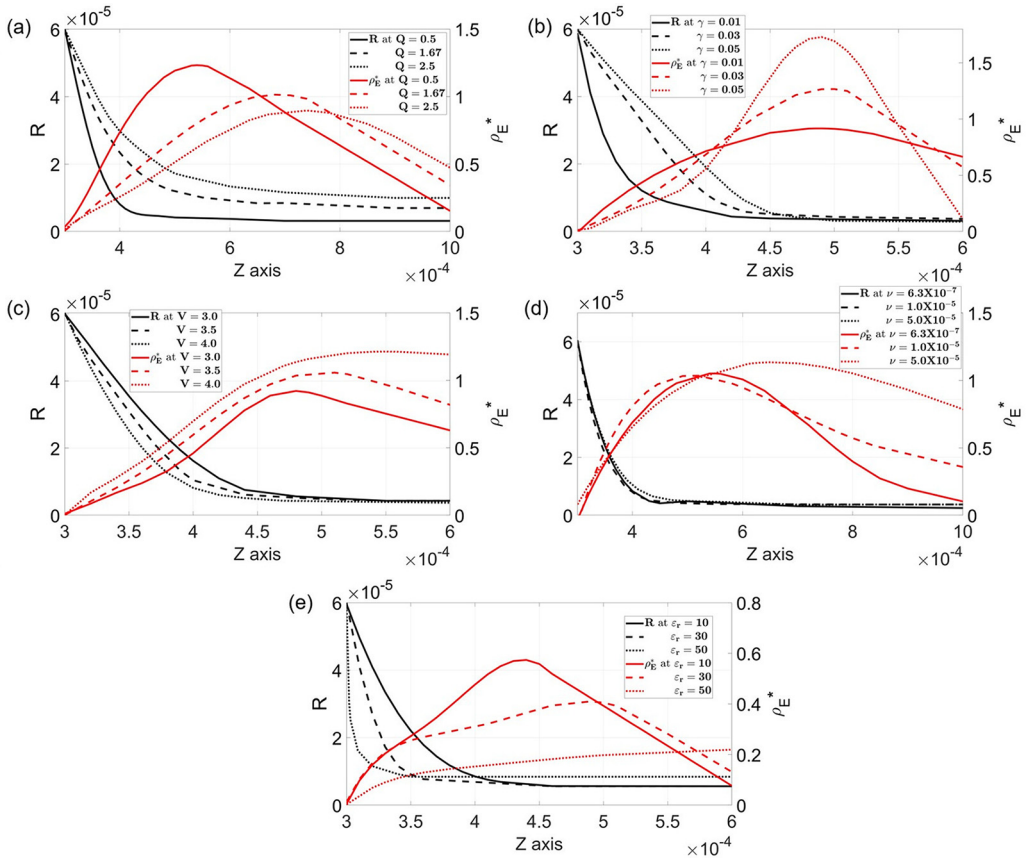

FIG. 6. Predicted distributions of cone-jet radius and charge density along the meniscus for heptane at varying (a) flow rates Q (mm^3/s), (b) surface tension coefficients, γ ($N\,m^{-1}$), (c) voltages, V (kV), (d) kinematic viscosities, $\nu(=\mu/\rho)$ (m^2/s), and (e) relative permittivities, ε_r.

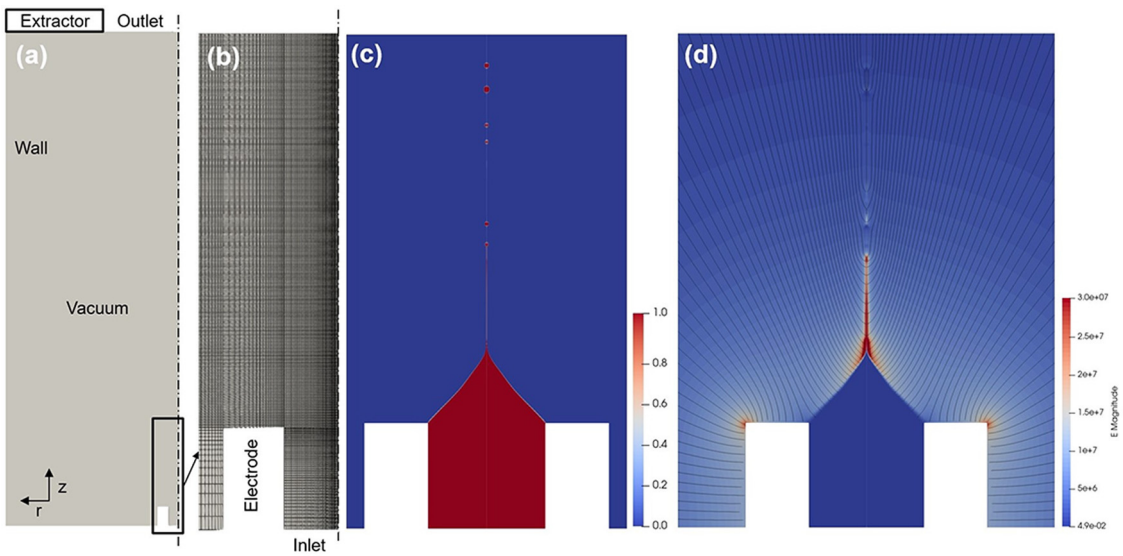

FIG. 7. Computation for TBP in steady cone-jet operation: (a) axisymmetric domain with 98 990 cells, (b) magnified emission region, (c) liquid volume fraction, and (d) magnitude and contour of the electric field.

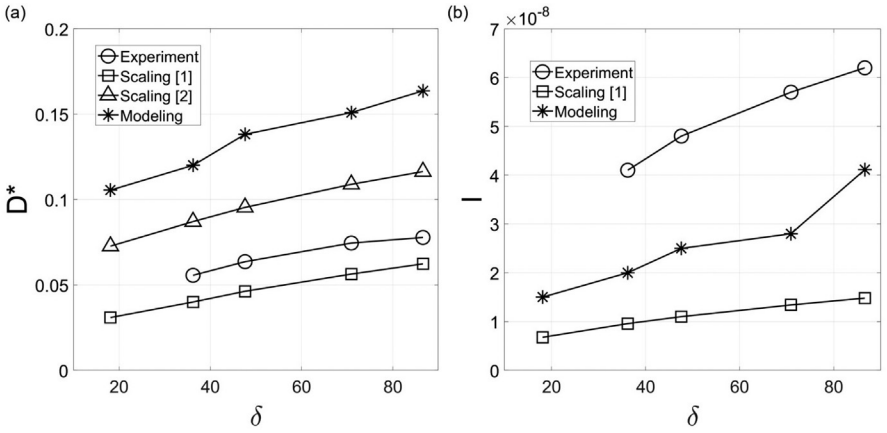

FIG. 8. Comparison of (a) dimensionless droplet diameters D^*, and (b) total currents I (A), by the experiment,[30] simulation, and scaling by Gañán Calvo[1] and De La Mora and Loscertales[2] with respect to varying δ for TBP ($\sigma = 2.3 \times 10^{-4}$ S m^{-1}).[6,8]

place mostly in the concave region where the electrostatic force dominates the surface tension and the viscous forces for moderate to high conductivity liquids. Low δ or high γ results in high charge density associated with high electrostatic force, leading to steeper menisci and smaller droplets. It is due to the geometrical constraint associated with transition of the meniscus from concave to convex according to the sign of the second-order derivative along the axis.

Note that ε_r varying from 8.91 to 30 shows a relatively constant meniscus in Fig. 9(c) unlike those for the low conductivity cases in Fig. 6(e). It is because the Coulombic force proportional to the charge density dominates the polarization force to determine the shape of the meniscus for moderate conductivity. The large relaxation time for $\varepsilon_r = 30$ suppresses charge transport to result in a jet radius of 265 μm much larger than 8.78 μm for $\varepsilon_r = 8.91$. It is also consistent with the result observed by Gamero-Castaño and Magnani that the normalized total current decreases from 2.5 to 2.0 for the relative permittivity increasing from 8.91 to 64.9 with no noticeable variation in the meniscus.[10]

The scaling equation for q_s in Eq. (22) suggests the surface charge independent of the flow rate high enough above the minimum $Q^* = \delta Re_E$, to maintain a stable cone-jet.[40] The results in Fig. 10(a) also support $\rho_{E,\max}$ insensitive to δ in the range, $\delta > 50$. Note the increasing effect of δ on $\rho_{E,\max}$ with increasing conductivity in Fig. 10(a). Similarly, decreasing $1/Re_E$ results in increasing charge density with such effect intensifying with increasing conductivity in Fig. 10(b).

The cone-to-jet length was scaled as $\frac{\gamma}{\varepsilon_0 E_t^2} \sim (\frac{\varepsilon_0^2 \gamma}{\rho \sigma^2})^{\frac{1}{3}} \delta$ in Gañán Calvo, where E_t is the tangential electric field.[6] The predicted results for the cone-to-jet length are fitted as $L_{cj} \sim \delta^{0.42}$ for heptane and as $L_{cj} \sim \delta^{0.58}$ for TBP in Fig. 11(a). Weaker dependence on δ for heptane is associated with lower charge density, resulting in a shorter L_{cj} than for TBP.

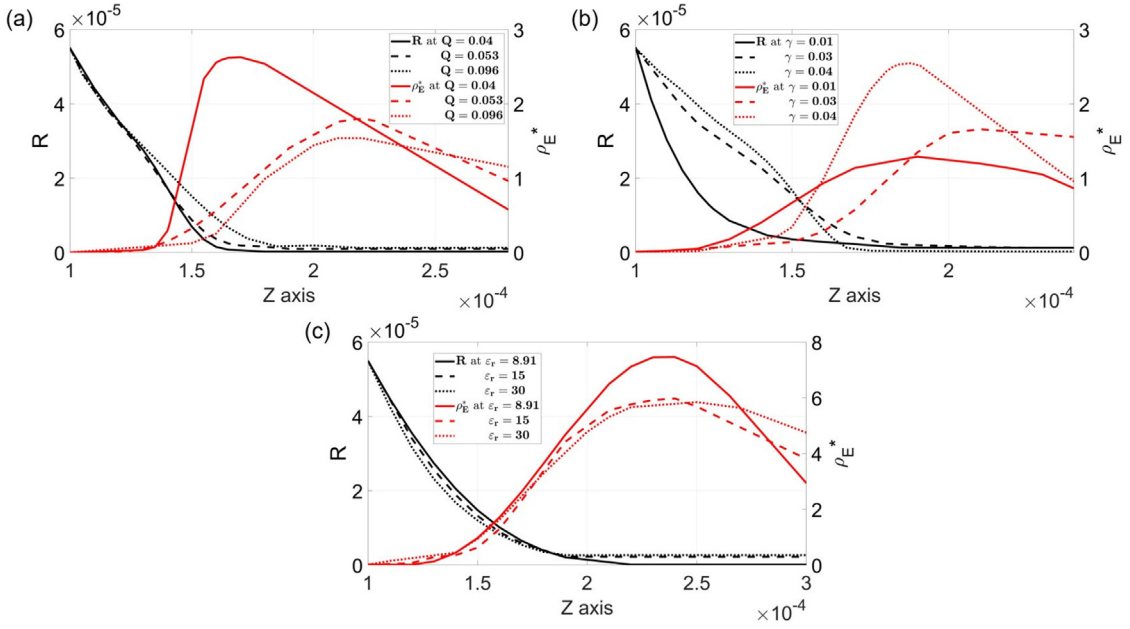

FIG. 9. Predicted distributions of cone-jet radius and charge density along the meniscus for TBP with respect to (a) Q (mm^3/s), (b) γ (N m^{-1}), and (c) ε_r.

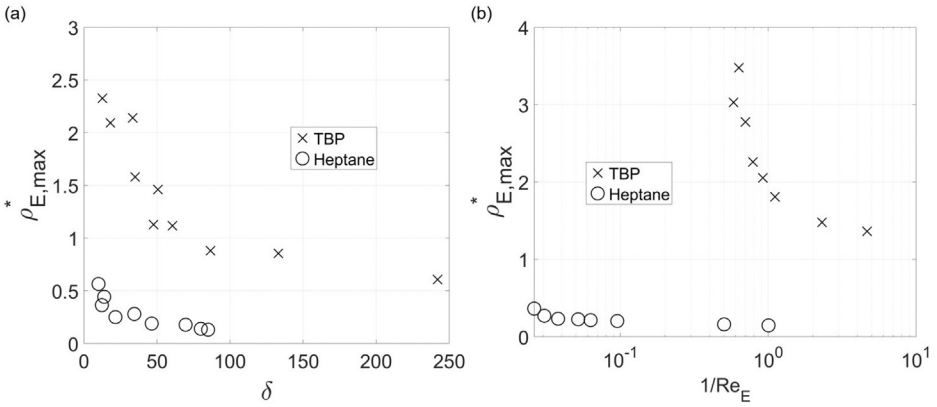

FIG. 10. Predicted maximum charge density at the cone-to-jet region as a function of (a) the dimensionless flow rate, δ, and (b) the inverse of electrical Reynolds number, $1/Re_E$.

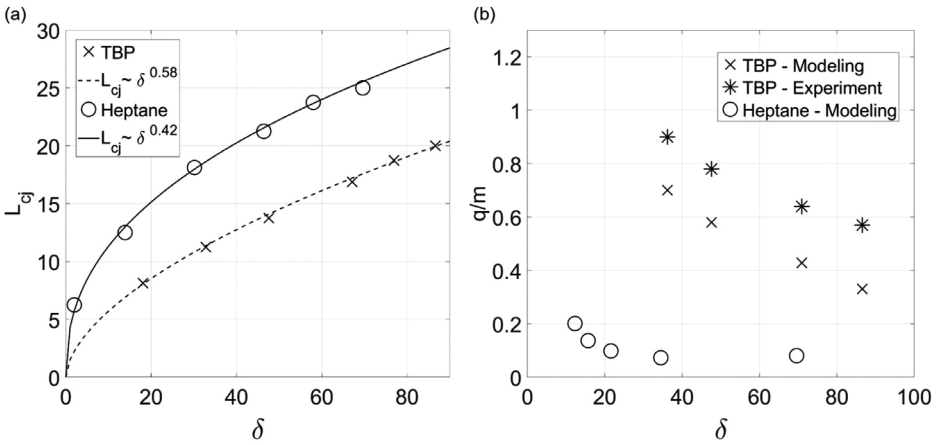

FIG. 11. Predicted (a) cone-to-jet length (μm) and (b) specific charge (C/kg) of the emitted droplets as a function of the dimensionless flow rate, δ.

Note lower $\rho_{E,\max}$ at the cone-to-jet region for heptane than for TBP in Fig. 11(a). The scaling, $L_{cj} \sim \delta^{0.58}$, fitted for TBP ($Re_E = 0.86$) shows stronger dependence than $L_{cj} \sim \delta^{0.17}$ from the BEM results in Gamero-Castaño annd Magnani.[10] It may be due to the emergence of a convex meniscus leading to higher charge density and a shorter L_{cj}, which is not taken into account in Gamero-Castaño and Magnani. In Fig. 11(b), the specific charge of the emitted droplets decreases with increasing δ, to support the experimental observations for moderate conductivity.[30] As a result, decreasing δ and increasing Re_E yields high charge concentration at the cone-to-jet region with shorter L_{cj} resulting in high specific charge (q/m) of the emitted droplets. Further work may be required to extend the new FVM to higher conductivity liquids, such as the ionic liquid, EMI-Im [1-ethyl-3-methylimidazolium bis(trifluoromethylsulfonyl)imide] employed in electric propulsion. For such high conductivity liquid the meniscus is expected to have a more convex conical shape[31] with an even shorter L_{cj}. High normal electric field, E_n, due to the increased charge density could explain possible ion evaporation at the high conductivity limit.[41–44]

V. CONCLUSION

We have developed the leaky dielectric EHD model in the open source FVM code, OpenFOAM. As compared with the BEM, the FVM can accurately predict the interface and multidimensional mechanisms, such as charge transport, internal flow, and droplet breakup, in an electrospray. Our new interface interpolation scheme for the VOF method allows conservation of electric charge and reproduces experimentally observed meniscus shapes in the cone-to-jet region. This interface scheme extends the FVM approach from low conductivity ($\sim 10^{-7}$ S m^{-1}, i.e., heptane) to moderate conductivities that are three orders of magnitude higher ($\sim 10^{-4}$ S m^{-1}). The new model is validated against droplet diameter, total current, and specific charge in good agreement with experiment and scaling laws for heptane and TBP in the literature. The results show the droplet diameter decreasing as the dimensionless flow rate decreases or as the electric Reynolds number increases. These are consistent with parametric investigation for the meniscus shape and the maximum charge density varying with the key operating conditions, i.e., flow rate and potential difference; and key liquid properties, i.e., conductivity, surface tension, viscosity, and relative permittivity. Decreasing charge density with increasing relative permittivity is explained in terms of the effect of larger relaxation time being dominant over that of a steep meniscus due to large polarization force. The results also show the meniscus changing from a concave to a convex shape toward vacuum with increasing maximum charge density and decreasing cone-to-jet length, as either the conductivity or the surface tension coefficient increases. A high charge density in the cone-to-jet

region leads to a high specific charge of emitted droplets with a high jetting velocity. Further work will be required to extend the FVM approach with the new interpolation scheme to more challenging ionic liquids of high conductivity such as EMI-Im [1-ethyl-3-methylimidazolium bis(trifluoromethylsulfonyl)imide].

ACKNOWLEDGMENTS

This effort was supported by a grant from NASA's Jet Propulsion Laboratory, California Institute of Technology to support the LISA CMT development plan (NASA/JPL Award No. 1580267), the Air Force Research Lab at Edwards AFB, CA (Award No. 16-EPA-RQ-09), and Air Force Office of Scientific Research (AFOSR) (Award No. FA9550-21-1-0067). The authors would like to thank Adam Collins and Peter Wright from UCLA, John Ziemer from NASA JPL, and David Bilyeu and Daniel Eckhardt from Air force Research Laboratory for their insightful discussions.

AUTHOR DECLARATIONS

Conflict of Interest

The authors have no conflicts to disclose.

Author Contributions

Henry Huh: Conceptualization (equal); Software (lead); Writing – original draft (lead); Writing – review & editing (equal). **Richard Edward Wirz:** Conceptualization (equal); Funding acquisition (lead); Supervision (lead); Writing – review & editing (equal).

DATA AVAILABILITY

The data that support the findings of this study are available within the article.

REFERENCES

[1]J. Zeleny, "The electrical discharge from liquid points, and a hydrostatic method of measuring the electric intensity at their surfaces," Phys. Rev. **3**, 69–91 (1914).
[2]M. Cloupeau and B. Prunet-Foch, "Electrohydrodynamic spraying functioning modes: A critical review," J. Aerosol Sci. **25**, 1021–1036 (1994).
[3]G. I. Taylor, "Disintegration of water drops in an electric field," Proc. R. Soc. London, Ser. A **280**, 383–397 (1964).
[4]J. R. Melcher and G. I. Taylor, "Electrohydrodynamics: A review of the role of interfacial shear stresses," Annu. Rev. Fluid Mech. **1**, 111–146 (1969).
[5]C. Pantano, A. Gañán-Calvo, and A. Barrero, "Zeroth-order, electrohydrostatic solution for electrospraying in cone-jet mode," J. Aerosol Sci. **25**, 1065–1077 (1994).
[6]A. M. Gañán Calvo, "On the general scaling theory for electrospraying," J. Fluid Mech. **507**, 203–212a (2004).
[7]A. Gañán-Calvo, J. Dávila, and A. Barrero, "Current and droplet size in the electrospraying of liquids. scaling laws," J. Aerosol Sci. **28**, 249–275 (1997).
[8]J. F. De La Mora and I. G. Loscertales, "The current emitted by highly conducting Taylor cones," J. Fluid Mech. **260**, 155–184 (1994).
[9]F. J. Higuera, "Flow rate and electric current emitted by a Taylor cone," J. Fluid Mech. **484**, 303–327 (2003).
[10]M. Gamero-Castaño and M. Magnani, "Numerical simulation of electrospraying in the cone-jet mode," J. Fluid Mech. **859**, 247–267 (2019).
[11]M. Herrada and J. Montanero, "A numerical method to study the dynamics of capillary fluid systems," J. Comput. Phys. **306**, 137–147 (2016).
[12]A. Ponce-Torres, N. Rebollo-Muñoz, M. A. Herrada, A. M. Gañán-Calvo, and J. M. Montanero, "The steady cone-jet mode of electrospraying close to the minimum volume stability limit," J. Fluid Mech. **857**, 142–172 (2018).
[13]I. Roghair, M. Musterd, D. van den Ende, C. Kleijn, M. Kreutzer, and F. Mugele, "A numerical technique to simulate display pixels based on electrowetting," Microfluidics Nanofluidics **19**, 465–482 (2015).
[14]H. Dastourani, M. Jahannama, and A. Eslami-Majd, "A physical insight into electrospray process in cone-jet mode: Role of operating parameters," Int. J. Heat Fluid Flow **70**, 315–335 (2018).
[15]J. López-Herrera, S. Popinet, and M. Herrada, "A charge-conservative approach for simulating electrohydrodynamic two-phase flows using volume-of-fluid," J. Comput. Phys. **230**, 1939–1955 (2011).
[16]M. A. Herrada, J. M. López-Herrera, A. M. Gañán Calvo, E. J. Vega, J. M. Montanero, and S. Popinet, "Numerical simulation of electrospray in the cone-jet mode," Phys. Rev. E **86**, 026305 (2012).
[17]S. Popinet, "Gerris: A tree-based adaptive solver for the incompressible Euler equations in complex geometries," J. Comput. Phys. **190**, 572–600 (2003).
[18]P. L. Wright and R. E. Wirz, "Multiplexed electrospray emission on a porous wedge," Phys. Fluids **33**, 012003 (2021).
[19]M. Sheikholeslami, "Numerical approach for MHD Al_2O_3-water nanofluid transportation inside a permeable medium using innovative computer method," Comput. Methods Appl. Mech. Eng. **344**, 306–318 (2019).
[20]A. Dogonchi, Z. Asghar, and M. Waqas, "CVFEM simulation for Fe_3O_4-H_2O nanofluid in an annulus between two triangular enclosures subjected to magnetic field and thermal radiation," Int. Commun. Heat Mass Transfer **112**, 104449 (2020).
[21]J. Brackbill, D. Kothe, and C. Zemach, "A continuum method for modeling surface tension," J. Comput. Phys. **100**, 335–354 (1992).
[22]C. Hirt and B. Nichols, "Volume of fluid (VOF) method for the dynamics of free boundaries," J. Comput. Phys. **39**, 201–225 (1981).
[23]H. Rusche, "Computational fluid dynamics of dispersed two-phase flows at high phase fractions,," Ph.D. thesis, Imperial College of Science, Technology and Medicine (2003).
[24]M. Aboukhedr, A. Georgoulas, M. Marengo, M. Gavaises, and K. Vogiatzaki, "Simulation of micro-flow dynamics at low capillary numbers using adaptive interface compression," Comput. Fluids **165**, 13–32 (2018).
[25]D. A. Hoang, V. van Steijn, L. M. Portela, M. T. Kreutzer, and C. R. Kleijn, "Benchmark numerical simulations of segmented two-phase flows in microchannels using the volume of fluid method," Comput. Fluids **86**, 28–36 (2013).
[26]H. Jasak and T. Uroić, "Practical computational fluid dynamics with the finite volume method," in *Modeling in Engineering Using Innovative Numerical Methods for Solids and Fluids*, edited by L. De Lorenzis and A. Düster (Springer International Publishing, Cham, 2020), pp. 103–161.
[27]Y. Okagaki, T. Yonomoto, M. Ishigaki, and Y. Hirose, "Numerical study on an interface compression method for the volume of fluid approach," Fluids **6**, 80 (2021).
[28]N. D. Vaughan, D. N. Johnston, and K. A. Edge, "Numerical simulation of fluid flow in poppet valves," Proc. Inst. Mech. Eng., Part C **206**, 119–127 (1992).
[29]K. Tang and A. Gomez, "Monodisperse electrosprays of low electric conductivity liquids in the cone-jet mode," J. Colloid Interface Sci. **184**, 500–511 (1996).
[30]M. Gamero-Castaño and V. Hruby, "Electric measurements of charged sprays emitted by cone-jets," J. Fluid Mech. **459**, 245–276 (2002).
[31]N. M. Uchizono, A. L. Collins, A. Thuppul, P. L. Wright, D. Q. Eckhardt, J. Ziemer, and R. E. Wirz, "Emission modes in electrospray thrusters operating with high conductivity ionic liquids," Aerospace **7**, 141 (2020).
[32]D. Kothe, W. Rider, S. Mosso, J. Brock, and J. Hochstein, "Volume tracking of interfaces having surface tension in two and three dimensions," in 34th Aerospace Sciences Meeting and Exhibit, 2012.
[33]J. Roenby, H. Bredmose, and H. Jasak, "A computational method for sharp interface advection," R. Soc. Open Sci. **3**, 160405 (2016).
[34]G. Tomar, D. Gerlach, G. Biswas, N. Alleborn, A. Sharma, F. Durst, S. Welch, and A. Delgado, "Two-phase electrohydrodynamic simulations using a volume-of-fluid approach," J. Comput. Phys. **227**, 1267–1285 (2007).
[35]M. Gamero-Castaño, "Electric-field-induced ion evaporation from dielectric liquid," Phys. Rev. Lett. **89**, 147602 (2002).
[36]J. Vila, P. Ginés, J. Pico, C. Franjo, E. Jiménez, L. Varela, and O. Cabeza, "Temperature dependence of the electrical conductivity in EMIM-based ionic liquids: Evidence of Vogel-Tamman-Fulcher behavior," Fluid Phase Equilib. **242**, 141–146 (2006).
[37]M. Gamero-Castaño, "Dissipation in cone-jet electrosprays and departure from isothermal operation," Phys. Rev. E **99**, 061101 (2019).

[38]A. Thuppul, A. L. Collins, P. L. Wright, N. M. Uchizono, and R. E. Wirz, "Mass flux and current density distributions of electrospray plumes," J. Appl. Phys. **130**, 103301 (2021).
[39]C. Ma and C. Ryan, "Plume particle energy analysis of an ionic liquid electrospray ion source with high emission density," J. Appl. Phys. **129**, 083302 (2021).
[40]A. M. Gañán Calvo, "The surface charge in electrospraying: Its nature and its universal scaling laws," J. Aerosol Sci. **30**, 863–872 (1999).
[41]S. W. Miller, B. D. Prince, R. J. Bemish, and J. L. Rovey, "Electrospray of 1-butyl-3-methylimidazolium dicyanamide under variable flow rate operations," J. Propul. Power **30**, 1701–1710 (2014).
[42]M. Gamero-Castaño and J. Fernández de la Mora, "Direct measurement of ion evaporation kinetics from electrified liquid surfaces," J. Chem. Phys. **113**, 815–832 (2000).
[43]D. Garoz, C. Bueno, C. Larriba, S. Castro, I. Romero-Sanz, J. Fernandez de la Mora, Y. Yoshida, and G. Saito, "Taylor cones of ionic liquids from capillary tubes as sources of pure ions: The role of surface tension and electrical conductivity," J. Appl. Phys. **102**, 064913 (2007).
[44]I. Romero-Sanz, R. Bocanegra, J. Fernandez de la Mora, and M. Gamero-Castaño, "Source of heavy molecular ions based on Taylor cones of ionic liquids operating in the pure ion evaporation regime," J. Appl. Phys. **94**, 3599–3605 (2003).